Outdoor Implied Current–Voltage Measurements of an Individual Encapsulated Cell in a Module

Raghavi Bhoopathy [ID], Oliver Kunz [ID], Robert William Dumbrell [ID], Thorsten Trupke [ID], and Ziv Hameiri [ID]

Abstract—**The performance of solar cells influences the reliability, lifetime, cost, and safety of photovoltaic power plants. The electrical performance of these cells, as well as, their degradation rates over time, can vary between individual cells within the same photovoltaic module. Current–voltage measurements can provide detailed data on cell performance, however, it cannot be performed on individual cells in encapsulated modules. In this study, we propose a contactless and nondestructive method that is based on Suns-photoluminescence measurements to extract the current-voltage characteristics of individual solar cells under operating conditions in the field. Applications of the method to identify the extent of various degradation mechanisms, such as light-induced and potential-induced degradation, are demonstrated and discussed. The main advantages of the proposed method include its low cost, and its fast and easy applicability.**

Index Terms—**Characterization.**

I. Introduction

RECENT years have seen a dramatic increase in utility-scale solar deployment [1] that has been driven by an extraordinary reduction in cost, particularly over the past decade [2], [3]. Utility-scale photovoltaic (PV) systems are now approaching gigawatts (GW) size and can contain millions of individual modules. The vast majority of systems have been installed in recent years [4], and hence, their long-term field performance is not well understood and needs to be studied. Outdoor diagnostic tools are required to serve this huge and rapidly growing industry, and to ensure optimal and safe operation of PV power plants.

Power degradation of PV modules is a major concern for PV power plant owners [5]. The degradation rate has a critical impact on the levelized cost of electricity and on the bankability of PV projects [6]. In particular, it is well understood that carrier induced degradation (CID) [7]–[10] and potential-induced degradation (PID) [11] can significantly reduce the power yield of PV installations [12]. Of particular significance is the fact that individual solar cells in a particular module do not degrade

consistently; often cells degrade at different rates [13]–[16]. Various factors, such as the cell and module structures, the silicon (Si) quality, the location of the cell within the module and the location of the module within the PV string can impact the degradation rate [15]. For example, solar cells located near the edge of a module and at the end of a string are those most detrimentally impacted by PID [11], [17].

Identifying the cause for the underperformance of individual cells is critical for detecting the corresponding source of power plant degradation. In many cases, early recognition of these fault mechanisms allows recovery measures to be quickly implemented [5]. In other cases, the results of such studies can inform the solar industry and provide important guidance for future cell and module designs.

Currently used characterization techniques, such as infrared (IR) thermography [18], [19], ultraviolet (UV) fluorescence [20], electroluminescence (EL) [21], [22], and photoluminescence (PL) imaging [23], [24] have proven to be helpful in identifying performance-limiting module faults. However, they all fail to provide *quantitative* information regarding the nature of each fault [25]–[27]. In order to investigate the different degradation modes and their causes, current–voltage (*I*–*V*) measurements of solar cells are generally highly desirable [28]. From such measurements, both the injection-dependent lifetime and the ideality factor can be obtained, leading to a more detailed understanding of the underlying detrimental recombination mechanisms [29].

Furthermore, it is challenging to extract the *individual* cell *I*–*V* information when cells are embedded in finished solar modules. Even with access to the module terminals, the commonly used Suns-V_{oc} method [30] cannot be applied to individual cells, as it is significantly affected by sunlight leaking into neighboring cells caused by total internal reflection through the module glass [28]. Another complication arises from the strong temperature sensitivity of the open-circuit (OC) voltage (V_{oc}) measurements (about -2.2 mV/°C), especially when measurements are performed outdoors [31]. For these reasons, either delaminating individual cells from a previously field-deployed module or electrically contacting through the ribbons by removing small areas of back sheet is undertaken to extract individual cell light *I*–*V* data. However, these procedures are destructive, time consuming, and not always successful [32].

Other methods to obtain *I*–*V* curves of a specific cell are either based on module-level *I*–*V* measurements, while changing the irradiance level on the tested cell [28], [33], [34] or using EL measurements in combination with dark lock-in thermography [32], [35]. The main limitation of these methods is the need to

contact the modules in order to inject current. Trained experts, as well as, sophisticated equipment and methods are often required, which either limits or even prevents their use for routine inspection of fielded modules.

In this study, we present a fast, simple, cost-effective, and contactless method to obtain implied *I–V* curves from encapsulated cells in field-deployed solar modules.

II. METHOD

A. Suns-Photoluminescence

The Suns-PL method [35]–[37] is used in this study to obtain implied *I–V* characteristics of solar cells that are free of series resistance (R_s) effects. During Suns-PL measurements, the tested solar cell is illuminated with varying intensity and the corresponding PL signal is measured simultaenously, while the solar cell operates at OC conditions. The light-generated current in the cell is linearly dependent on the illumination intensity, while the cell's implied OC voltage (iV_{oc}) is related to the measured PL signal (Φ_{PL})

$$iV_{oc} = V_T \ln\left(C\phi_{PL}\right) \tag{1}$$

where V_T is the thermal voltage of about 25.8 mV at 26.85 °C and *C* is a calibration constant mainly dependent on the optical characteristics of the tested structure. Key benefits of this method include the following.

1) The method is *contactless*, hence, avoiding the requirement to access individual cell or module terminals.
2) Highly sensitive implied voltage measurements in the operational voltage range (between maximum power point, MPP and OC) are achieved through PL, as the measured signal is exponentially related to iV_{oc}.
3) The measurement is *insensitive* to temperature changes, which is beneficial for outdoor measurements [36].

B. Calibration Procedure

Although Suns-PL measurements can be used without calibration to identify different loss and cell failure mechanisms, a few applications might be required to obtain calibrated absolute implied *I–V* curves. The illumination intensity of the light source is calibrated to the respective Suns by measuring the short-circuit current (I_{sc}) of a reference cell having a similar quantum efficiency to the cell being measured. The calibration of the implied voltage is achieved by determining the factor *C* [of (1)] which can be obtained using two different approaches.

1) Suns-Photoluminescence Curves: The first approach is based on Suns-PL measurements of a statistically significant sample set in a string. In this method, the PL response of some of the cells in a string is measured (measured cells) using the setup described later in Section II-C. The sample set is selected such that it is large enough to represent most of the cells in the string. The temperature corrected string voltage is given by

$$V_{oc,\text{string}} = \left[\sum_{i=1}^{M} V_T \ln\left(\frac{\phi_i}{C}\right)\right] + \left[(N-M)\,V_T \ln\left(\frac{\bar{\phi}_{1-M}}{C}\right)\right] \tag{2}$$

where *M* is the number of measured cells in the string, *N* is the total number of cells in the string, Φ_i is the integrated PL intensity of the *i*th cell measured at one Sun illumination and $\Phi_{1\text{-}M}$ is the average PL intensity of all the measured cells (from 1 to *M*) at the same illumination (one-Sun). In this equation, the first and second terms represent the sum of V_{oc} of measured and unmeasured cells, respectively, from (1).

Using (2), *C* is calculated as [22], [35], [37]

$$C = \sqrt[N]{\frac{\left(\bar{\phi}_{1-M}\right)^{N-M}}{\exp(V_{oc,\text{string}}/V_T)}\prod_{i=1}^{M}\phi_i}. \tag{3}$$

2) Luminescence Imaging: Luminescence images, such as EL [22], [35], [37] or PL [23], [24], [38]–[40] can also be used to determine *C* using (3), where Φ_i is a pixel value representing the luminescence intensity of the *i*th cell after flat-field correction. In this study, we select Φ_i as the maximum pixel value of the *i*th cell (after eliminating the top 0.1% intensity pixels, that could be measurement artifacts because of "hot pixels," saturated pixels, or faulty pixels [41]). To allow comparison between the two methods, one of the measured Φ_i is normalized using the one-Sun PL intensity from the Suns-PL measurement of the same cell. This is done to minimize the impacts the optical parameters have on the two methods (luminescence imaging and Suns-PL; each is impacted differently by these parameters). Note that any cell can be selected for this calibration procedure. Although using luminescence images is quicker compared with Suns-PL for calibrating Suns-PL curves, it is comparatively complicated and requires more sophisticated equipment. However, if the plant was already inspected with luminescence imaging, the images can then also be used for calibration.

If EL images are used, the image should be obtained with minimum influence of R_s, i.e., typically at low current injection ($<0.1\ I_{sc}$) [22], [35], [37]. Note that EL, in contrast with PL, requires contacting either the string or module terminals to inject current.

Using the temperature-corrected module V_{oc} ($V_{\text{mod},oc}$) instead of $V_{\text{string},oc}$ (as presented in [22], [35], and [37]) in the above two approaches might lead to a smaller number of cells needing to be measured, thus, making it less time consuming. However, measuring $V_{\text{mod},oc}$ is, in general, not practical for fielded modules as it requires disconnecting the modules from the string, a procedure which requires a qualified (and expensive) electrician. It is possible to estimate $V_{\text{mod},oc}$ either by using information provided in the datasheet of the investigated module or by measuring $V_{\text{mod},oc}$ of an equivalent module of the same type and by including typical module degradation rates.

On the other hand, $V_{\text{string},oc}$ can be measured by the string inverter, as many of them have the capability to measure at least a part of the *I–V* curve of the string [43]. The additional advantage of this is that the *C* estimated for one of the strings in a PV plant can be used for the entire plant as it is not expected to significantly vary for the same module type and technology.

C. Experimental Setup

Fig. 1 presents a schematic of the Suns-PL system developed as part of this study.
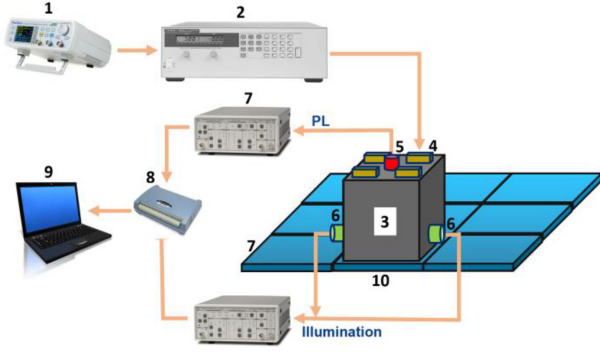
Fig. 1. Schematic of the Suns-PL measurement system with (1) signal generator, (2) power supply, (3) Suns-PL tool, (4) high-power LED arrays, (5) InGaAs photodiode with optical filtering, (6) Si photodiodes, (7) transimpedance preamplifiers, (8) data acquisition system, (9) computer, and (10) encapsulated solar cell in a module.

Fig. 2. Outdoor PL image of the nine-cell minimodule used in this study (cell IDs are given in red).

TABLE I
CELL AND MODULE PARAMETERS

Cell ID	V_{oc} [mV]	I_{sc} [A]	R_{sh} [kΩ cm^2]	FF [%]	η [%]
1	666	9.05	0.33	65.51	16.41
2	633	8.94	1.11	70.96	15.94
3	624	8.75	0.21	63.63	13.54
4	651	9.04	1.61	69.97	16.46
5	648	8.83	4.24	57.58	13.11
6	673	9.16	4.48	72.60	17.76
7	667	9.31	0.96	71.44	17.82
8	633	8.92	3.62	70.87	15.97
9	646	8.98	1.89	67.28	15.55
Mean	649	9.00	2.05	67.76	15.84
σ	16	0.17	1.65	4.84	1.63
Module	**5,810**	**8.73**	**4.71**	**68.69**	**15.99**

The variable light source is comprised of four 500 W warm-white light emitting diode (LED) arrays (4) mounted to heat sinks. Heat absorbing KG3 glass filters [42] are attached in front of the LEDs to effectively cutoff infrared wavelengths greater than approximately 900 nm. The maximum light intensity that can be achieved with this tool is slightly higher than seven Suns (at the sample surface), while the minimum intensity is in the order of 2.5×10^{-3} Suns. Note that the Suns-PL tool (3) is placed on top of the measured cell (10). The inner surfaces of the tool are highly reflective to maximize the illumination intensity reaching the cell. The LEDs are operated in current control mode using a power supply [(2); model HP6575A [43]] that is controlled by a signal generator (1).

In between the LED arrays, an indium gallium arsenide (In-GaAs) photodiode (5) is mounted, along with a suitable optical filter set (cuton and cutoff wavelengths of 1100 and 1150 nm, respectively [21]) to measure the PL intensity with minimal impact of stray light in outdoor conditions. Note that the height of the Suns-PL tool (25 cm) is designed as a tradeoff between the InGaAs photodiode capturing the PL signal from the entire tested cell and receiving sufficient amount of PL signal (that drops off proportional to the square of the distance). In this tool, the collection efficiency of the PL signal between the center and edge of the cells differs by ∼16% according to the cosine-fourth-power law that applies in such circumstances. The tool contains two Si photodiodes (6) that are mounted on its inner walls pointing upward to ensure that they only measure the illuminating light and not the light reflected from the measured sample (Fig. 1 indicates only the output connections of these photodiodes, not their actual locations, situated inside the tool). The measured photocurrents from the InGaAs and Si photodiodes are amplified using SR570 low-noise transimpedance preamplifiers (7) [44]. The preamplifier signals are then captured by the data acquisition card (8); USB-1808 from Measurement Computing [45]) and transferred to the computer (9) for further processing (see Fig. 1).

D. Minimodule

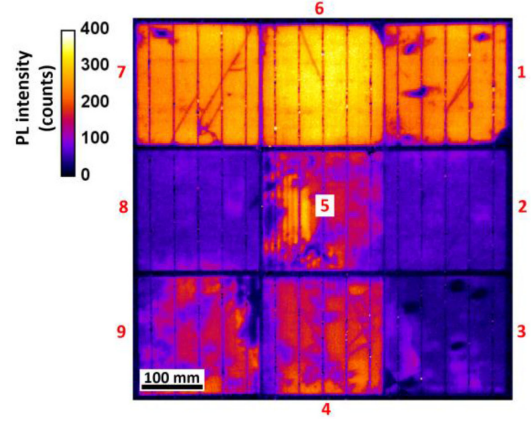A minimodule consisting of nine cast-monopassivated emitter rear totally diffused (PERT) silicon solar cells connected in series is used in this study. To highlight the importance of measuring individual cell characteristics, we selected cells with different types of defects in order to increase module nonuniformity. We also induced shunts with different levels of severity to Cells 1, 3, and 7 by scratching the rear of the cells with a diamond pen. An outdoor PL image [23] of the minimodule obtained at approximately one Sun illumination is shown in Fig. 2. To validate the method, the module was built to enable access to the terminals of each individual cell. This allows us to perform Suns-V_{oc} (alongside Suns-PL measurements) and light I–V measurements of individual cells. Light I–V measurements on each cell were performed after encapsulation using a SPIRE module flash tester [46]. The electrical parameters of the individual cells are summarized in Table I.

III. RESULTS AND DISCUSSION

A. Comparison Between Calibration Methods

Fig. 3 presents the implied voltage calculated from different methods using (3), as detailed in Section II-B, while all cells in the minimodule ($T = M = 9$) are measured. Note that in the presented case, V_{mod} is identical to V_{string} as this module is not connected to other modules. The voltages are measured using a SPIRE module flash tester [46] and are corrected to
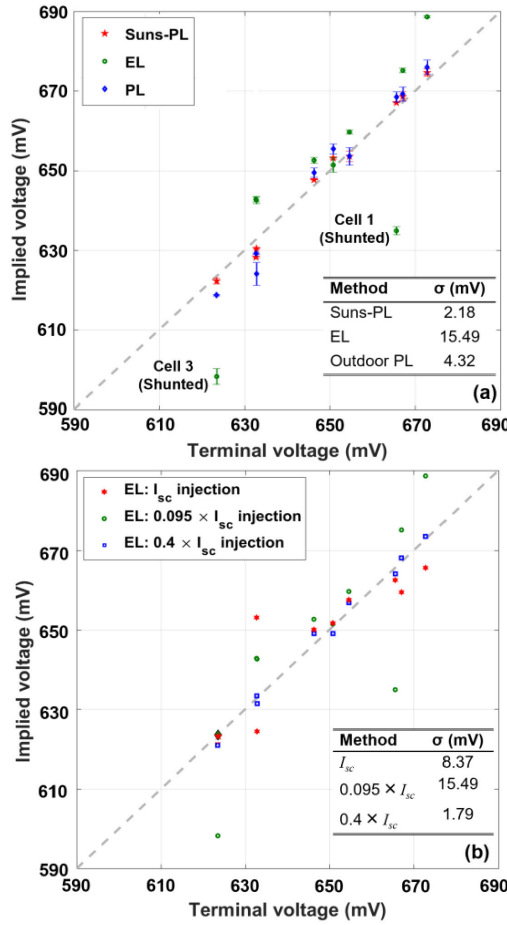
Fig. 3.   Implied voltage as a function of terminal voltage using (a) different calibration methods and (b) calibration based on EL images taken at different current injection levels. The dotted line represents $y = x$, while the standard deviation (σ) between $V_{\text{ter}}-V_{\text{imp}}$ for each method is displayed in the inserted tables. Error bars in (a) are obtained from five repeat measurements.
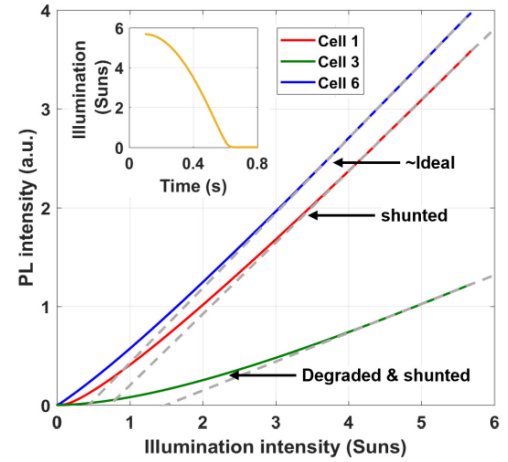
Fig. 4.   Measured PL intensity of three selected cells from the minimodule as a function of illumination intensity. The inset shows the illumination intensity as a function of time. The dashed line represents the linear relationship that is observed at high illumination intensities.

recombination at this injection range. Fig. 3(b) presents a comparison between implied voltages calculated from EL images measured with forward current equivalent to I_{sc}, $0.4 \times I_{sc}$, and $0.095 \times I_{sc}$. In this case, even the measurement with the highest current, with a significant impact of R_s, performs better than the low injection measurement. The midrange current injection of $0.4 \times I_{sc}$ provides the best results for this particular module with a very low σ of 1.62 mV from the terminal voltage.

Note that in the field, the accuracy of the methods will depend on the sample set measured for the estimation of C. The main advantage of Suns-PL-based calibration is its simplicity, as it avoids the need for additional equipment. Therefore, in this study, we have used Suns-PL measurements for calibration purposes whenever absolute implied voltages are calculated from luminescence measurements.

B. Indoor Measurements

We first demonstrate the proposed method in the laboratory, as indoor measurements can be performed with a well-controlled low-level surrounding illumination. These measurements will later be used for comparison with outdoor measurements. During the measurement, the illumination intensity incident on the measured cell is varied approximately sinusoidally with a frequency of 0.45 Hz, as shown in the inset in Fig. 4. Such a slow frequency allows for low-noise quasi-steady-state measurements that minimize measurement artifacts that could be present, in particular when measuring high-efficiency solar cells with long carrier lifetimes [47]–[49].

Fig. 4 displays the PL signals of three cells with significantly different *I–V* characteristics (Cells 1, 3, and 6 from the minimodule shown in Fig. 2). Note that any fault affecting the implied *I–V* curve, such as cell degradation, is reflected in the luminescence signal [50]. For an ideal cell, a linear relationship between illumination intensity (hence, the current) and emitted PL intensity (hence, the exponential of voltage) is expected. As these curves are fitted for high illumination intensities, it is expected they are mostly impacted by the diode with unity

26.85 °C. The inserted table presents the standard deviation (σ) of the difference of implied and terminal voltages, for all the cells and for each method. The σ values can be interpreted as the root-mean-square-error (RMSE) deviation. The Suns-PL measurements are performed using the setup described in Section II-C, while the EL and PL measurements are performed using the setup described by Bhoopathy *et al.* [38]. The PL imaging is performed by modulating the module operating conditions between MPP and OC, while EL presented in Fig. 3(a) is performed at a low injection of $0.095 \times I_{sc}$.

The results indicate that a calibration based on Suns-PL data for all cells against V_{mod} provides the most accurate results when following the method based on outdoor PL. The slightly larger σ of the outdoor PL method is attributed to the small impact of R_s at MPP. The calculated voltage using EL images under low current injection of less than 10% of I_{sc} ($0.095 \times I_{sc}$) as proposed in [22], [35], and [37] is erroneous, especially in the case of heavily shunted cells (see Cells 1 and 3). This is because the low-injection measurements are subject to significant shunting and high ideality factor recombination. Hence, a tradeoff needs to be found between the benefits of low injection measurements to reduce the impact of R_s and the impact of shunt and nonideal

Fig. 5.   *I–V* curves obtained from Suns-PL (iV_{oc}) and Suns-V_{oc} (V_{oc}) measurements.

TABLE II
TWO-DIODE MODEL FIT PARAMETERS

Cell ID	J_{01} [pA/cm^2]	J_{02} [nA/cm^2]	R_{sh} [kΩ cm^2]	pFF [%]
1	0.1	35	0.3	74.86
3	0.2	133	0.5	72.89
6	0.1	16	$1×10^9$	81.21

ideality factor (in the absence of R_s). Therefore, for this ideal case, the fit intercept is expected to be at the origin. For the nonideal case, where the curve cannot be described by only one diode, the intercept is expected to shift from the origin. For instance, in the case of the best cell (Cell 6), the relationship between the emitted PL intensity and illumination intensity is linear throughout most of the measurement, and thus, the distance of the intercept from the origin is small.

For shunted cells, the linear relationship fails at illumination intensities <0.5 Suns with reduced PL signal throughout the measurement, although the slope remains similar (Cell 1 in comparison with Cell 6). This is a clear demonstration for the ability of the proposed method to detect shunts, such as those produced by PID [11]. Early detection of these shunts can be useful in order to recover the affected modules in the field [11], [12], [17]. Although Cells 1 and 3 have similar shunt resistances (R_{sh}), the slope of the PL intensity reduces significantly for Cell 3 as it is highly degraded. This highlights the ability of the proposed method to detect increased saturation currents in solar cells, for example, cells that are affected by CID [51].

Fig. 4, thus, highlights the ability of the Suns-PL method to detect different loss mechanisms and to distinguish between them, even *before* calibrating the measured PL intensity to an absolute implied voltage. A more detailed discussion regarding the prevalent loss mechanisms is presented in Section III-C. It should be noted that in many cases, it is not necessary to calibrate the Suns-PL measurements to absolute *I–V* curves (via the determination of *C*). For instance, if the purpose of the measurement is either a *relative* comparison between cells or identification of fault mechanisms, then the uncalibrated Sun-PL data already provide sufficient information.

C. Validation by Suns-V_{oc} Measurements

Using *C* values determined from Suns-PL measurements of all nine cells of the minimodule (as presented in Section III-A), the Suns-PL measurements of the three cells are converted into implied *I–V* curves and presented in Fig. 5. As expected from the

PL image (see Fig. 2) and the measured PL signal (see Fig. 4), the difference between the *I–V* curves of the three cells is significant.

To validate the method, Fig. 5 also includes the measured Suns-V_{oc} [30] curves of the same cells. Note that the Suns-PL data are denser at illumination intensity less than 1.5 Suns, since each cell's Suns-PL curve is taken using two separate sweeps to increase the measurement range. The measured terminal voltages V_{oc} agree very well with the iV_{oc} determined by the Suns-PL method. The deviation between the corresponding curves, observed above one-Sun intensity, stems most likely from shading and contact recombination induced by the front metal grid, in combination with the lateral R_s of the cell, as previously reported [54]. This deviation is found to be 4.5–5 mV at one Sun for the cells tested here. A similar value was previously reported in [54]. Note that because of the rapid decrease of the PL signal with voltage, the Suns-V_{oc} measurements extend into a lower voltage regime. However, the range covered using Suns-PL is fully adequate to obtain all the relevant solar cell parameters, as will be shown below. It is possible to translate the light intensity to current, if I_{sc} is known. However, it is challenging to measure I_{sc} of encapsulated cells. To minimize the associated uncertainty, in this study, we use the light intensity and not I_{sc}.

The *J–V* characteristics of a solar cell without the influence of R_s can be described by the two-diode model [52], [53]

$$J = J_L - J_{01} \left(\exp\left(\frac{V}{m_1 V_T} \right) - 1 \right)$$
$$- J_{02} \left(\exp\left(\frac{V}{m_2 V_T} \right) - 1 \right) - \frac{V}{R_{sh}} \qquad (4)$$

where J_L is the light-generated current density, J_{01} (J_{02}) are the saturation current densities of the diode with ideality factors $m = 1$ ($m = 2$), and *V* is the implied or terminal voltage. In many cases, extracting the two-diode model parameters allows identification of the dominant recombination mechanisms [53]. In Fig. 6(a), the two-diode model fits (using weighted least squares [54], [55]) to the iV_{oc} data are presented. Reasonable fits are obtained for Cells 1 and 6 compared with Cell 3 that could not be fitted well at low voltages. Fig. 6(b) provides an example for the capability to extract the two-diode model parameters from the measurements. The figure presents the obtained currents flowing through the different components (two diodes and shunts) of Cell 1. Obtaining these parameters can be useful when investigating fundamental recombination processes within a solar cell [55]. The fit parameters are summarized in Table II. It is noticeable

Fig. 7. Implied *I–V* curves of Cell 7 measured indoor and outdoor under different shading conditions; PL intensity as a function of illumination intensity is shown as an inset.
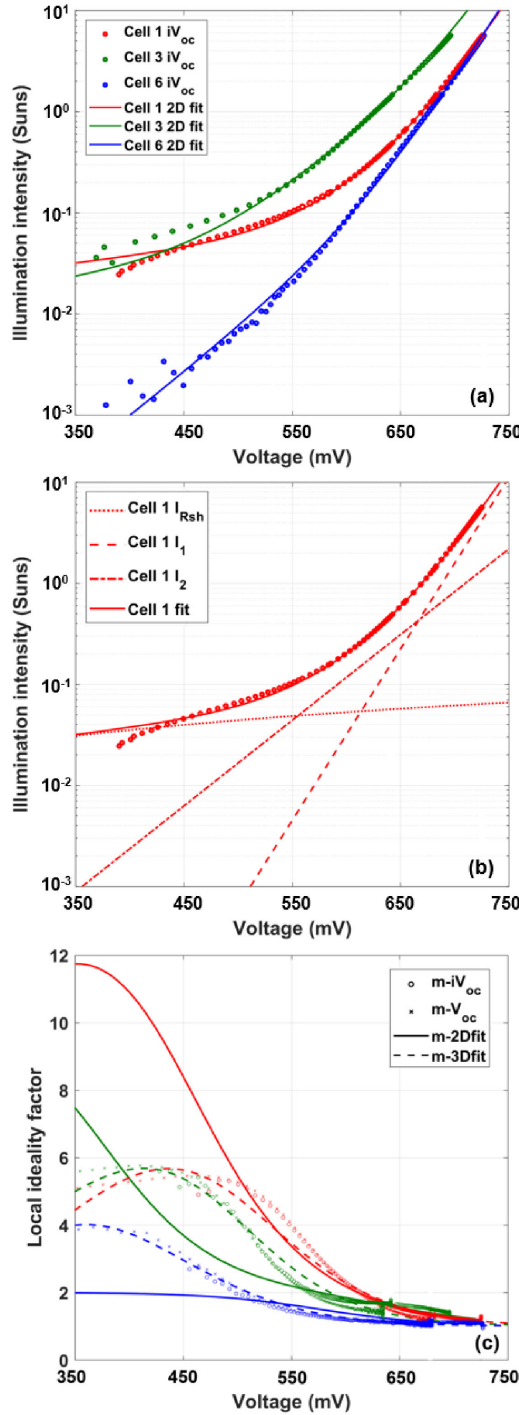

Fig. 6. (a) Semilog plot of iV_{oc} with two-diode model fits. (b) Semilog plot showing the two-diode model fit along with its individual components for Cell 1. (c) Local ideality factor of iV_{oc} and V_{oc}, together with their two-diode and three-diode model fits.

and 3 is significantly low, similar to the findings from the *I–V* measurement (see Table I). However, there is a significant difference between the R_{sh} of Cell 3 obtained by the two methods. This discrepancy is probably because of the unreliable fit for this cell at low illumination intensities.

In order to gain additional information, the local ideality factor as a function of voltage (the *m–V* curve) is calculated using

$$m = \frac{dV}{d \ln(J_L) \times V_T}. \qquad (5)$$

Such *m–V* curves can be very useful, since the efficiency limiting degradation mechanisms in a solar cell are not always obvious from standard *I–V* curves [29], [55]–[57]. The *m–V* curve reveals more information by highlighting the shape of the *I–V* curve that might otherwise go unnoticed [29].

Fig. 6(c) presents the *m–V* curves obtained by Suns-PL (*m–iV_{oc}*), Suns-V_{oc} (*m–V_{oc}*) measurements, together with their corresponding two-diode model fits (*m–2Dfit*). The good agreement between the *m–iV_{oc}* and *m–V_{oc}*, even for such a sensitive parameter (as *m* is calculated from the derivative of the measured data), strongly validates the proposed method. However, the measurements cannot be fitted by the two-diode model, revealing the limitation of this model. This is because the simplified standard two-diode model fit does not capture other recombination processes, such as the resistance-limited enhanced recombination [58].

Fig. 6(c), therefore, also includes the fits obtained by a three-diode model (*m–3Dfit*) without the influence of R_s whose equivalent circuit is given in Fig. 7 and *J–V* characteristics is given by

$$J = J_L - J_{01} \left(\exp \left(\frac{V}{m_1 V_T} \right) - 1 \right)$$
$$- J_{02} \left(\exp \left(\frac{V}{m_2 V_T} \right) - 1 \right) - J_H - \frac{V}{R_{sh}} \qquad (6)$$

where $J_H = J_{0H}(\exp(\frac{V_H}{m_H V_T}) - 1)$ and $V_H = V - R_H J_H$ and J_{0H} is the saturation current density of the diode with ideality

that the extracted J_{02} of Cell 3 is larger compared with the other cells. Hence, the influence of the depletion region or edge recombination extends to a larger voltage range. As this extends beyond MPP, there is a subsequent reduction in the cell efficiency.

Furthermore, the larger total recombination current of Cell 3 leads to a strongly reduced V_{oc}. The extracted R_{sh} of Cells 1
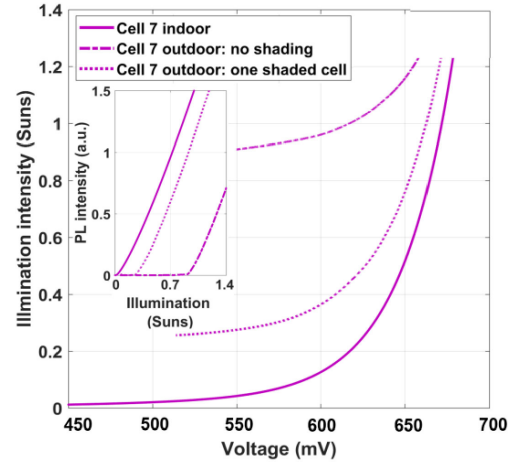
TABLE III
THREE-DIODE MODEL FIT PARAMETERS

| Cell ID	J_{01} [pA/ cm^2]	J_{02} [nA/ cm^2]	R_{sh} [kΩ cm^2]	J_{0H} [nA/ cm^2]	R_H [kΩ cm^2]	pFF [%]
1	0.1	36	2.6	18.9	0.1	72.87
3	0.4	75.7	0.8	26.5	0.1	71.57
6	0.1	7.6	1×10^9	2.7	4	82.59

Fig. 8. Equivalent circuit model of the three-diode model comprising of the standard two-diode model representing the main body of the cell and a third diode series connected via a resistor representing a region of enhanced recombination [29].

factors $m = H$. These fits match the measured data significantly better.

The extracted three-diode model fit parameters are summarized in Table III. The height and extension of the hump in the m–V data are related to the recombination current (J_{0H}), whereas the hump position is correlated with the resistance (R_H) that separates the localized recombination regions from the remaining regions of the solar cell [29]. The humps of Cells 1 and 3 are higher and extend over a larger voltage range, which indicates higher J_{0H}. For Cell 3, even at very high voltages (690 mV), m is greater than one, implying that, even in this voltage range, the recombination is not solely dominated by J_{01}. We assume that the localized dark spots in the PL image of this cell (as presented in Fig. 2) lead to localized recombination regions.

D. Outdoor Measurements

In this section, the application of the proposed Suns-PL method for outdoor measurements is discussed. Here, the fact that modules are operated at MPP causes extra complications. As Suns-PL measurements require OC conditions [59], [60], they can easily be performed at night time, when no cell produces power, and hence, no current is flowing. However, night measurements are undesirable because of safety and practical considerations. For day measurements under sunlight irradiation, while the module is biased by the MPP tracker, power is extracted from the module. In the context of outdoor PL imaging, we recently presented a contactless method to force the investigated cells into the OC condition [23]. The method is based on shading a cell in a series connected substring, reducing the current through the corresponding substring to approximately zero, and thus, engaging the corresponding by-pass diode [39]. The same approach is used here for Suns-PL measurements. Using the fabricated minimodule, the proposed Suns-PL method is tested (using the setup described in Section II-C) under approximately one-Sun daylight illumination, while the module is biased with an electronic load such that the MPP power is extracted.

Fig. 7 displays indoor and outdoor Suns-PL measurements of Cell 7 (a weakly shunted nondegraded cell). As can be seen, there is a large discrepancy between the measurements, causing an offset in the implied I–V curves. This significant difference arises because of the investigated cell (test cell) not being under OC conditions during the measurement since some current still flows through all the cells. This current will be highly variable
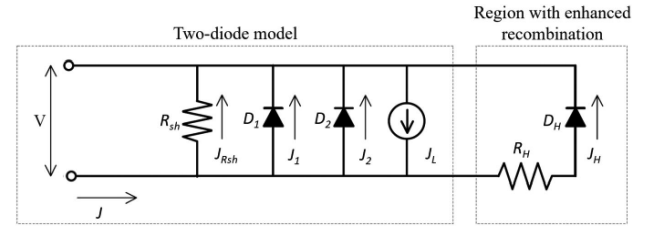
and change with the illumination intensity on the test cell as it receives the minimum illumination in the substring until it reaches the MPP current (I_{MPP}). The tested cell, which is shaded by the measurement system ("Cell 7 outdoor: No shading"), responds only when the light-induced current exceeds I_{MPP} (when test cell illumination is greater than other series-connected cells), as can be seen with the inset of Fig. 8.

The situation is expected to be improved by shading additional cells in the same string. When one additional series-connected cell is shaded (Cell 1 was used here as an example), we expect the investigated cell (Cell 7) to be forced to the OC condition in an ideal case. In this case, the obtained implied I–V curve should be similar to that obtained indoors. However, as can be seen in Fig. 8 ("Cell 7 outdoor: One shaded cell"), there is still a significant difference compared with the indoor measurements. This can be explained by either one or a combination of the following reasons.

1) Shunt conductance in the shaded cell.
2) Light leakage into the shaded cell from the unshaded module areas.
3) Light leakage into the cell under test from unshaded module areas.

In order to investigate the impact of the shunt conductance on the I–V curve offset, different cells in the minimodule are shaded, while the actual Suns-PL measurement is performed on Cell 7. The results of this measurement are presented in Fig. 9(a).

To understand this, we need to consider that a shaded cell is reverse biased by the nonshaded cells, and therefore, if shunted, allows a current to flow through the series-connected nonshaded cells (including the test cell). Thus, a shunted shaded cell prevents the test cell from reaching the OC condition, causing an offset in the measured I–V curves that depends on the level of shunting present in the shaded cell. In Fig. 9(b) the relationship between shunt conductance (based on the measured R_{sh} of Table I) and the offset in the I–V curves [measured at 550 mV, see dashed vertical line in Fig. 9(a)] are presented. We observe a roughly linear relationship between illumination offset and shunt conductance in accordance with our expectation. However, even when a nonshunted and nondegraded cell (Cell 6) is chosen as the shaded cell [blue curve in Fig. 9(a)], the implied I–V curve still has a significant offset which is caused by light leakage into the shaded cell from the surrounding areas.

We assume that a small amount of light is penetrating into the shaded cell via internal reflection of sunlight through the
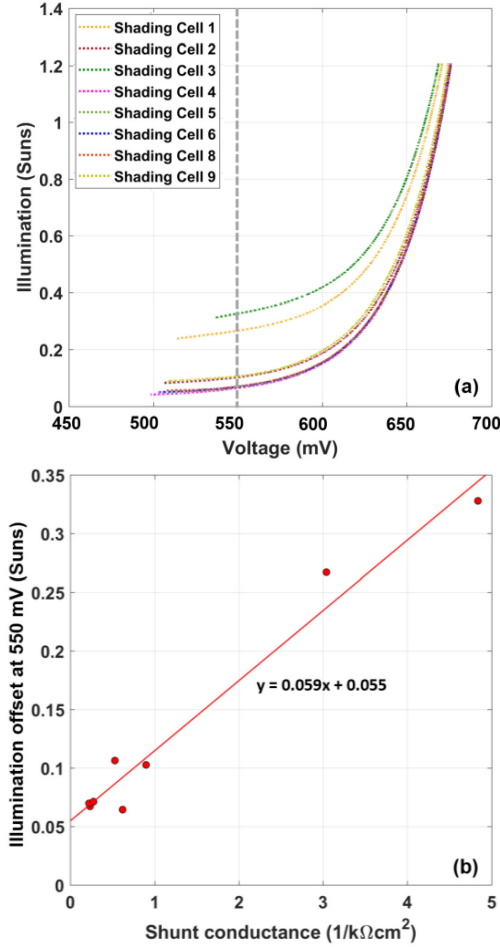
Fig. 9. (a) Measured implied *I–V* curves of Cell 7, while other cells are individually shaded. (b) Illumination offset at 550 mV [represented by vertical dashed line in (a)] as a function of the shunt conductance of the shaded cell.

Fig. 10. Outdoor implied *I–V* measurements obtained with extended shading.

module glass [28]. In our measurements, the offset is found to be approximately 0.055 Suns [0.49 A, see Fig. 9(b)]. The value observed is not always the same and is influenced by the shading technique used. Another source of error in this measurement is light leaking into the test cell. As a result, the penetrating light reaches the PL detector and causes a small constant offset in Φ_{PL}. This has very little impact on the voltages measured at higher illumination intensity but could dramatically alter the lower voltage region of the curve (at lower light intensities). Therefore, Φ_{PL} is corrected for all the measurements presented here by shifting the measured PL signal by the offset in measured PL intensity when the LEDs are OFF.

To address these challenges, the shading is extended to cover an area slightly larger than the eight neighboring cells around the test cell (around 20 cm from the edge of the test cell). This has three effects: 1) it eliminates the PL offset mentioned above because of the light leaking into the test cell; 2) it effectively reduces light leakage into the shaded cells; and 3) it dramatically reduces the leakage current via shunt conductance since more cells are shaded and the reverse voltage caused by the shading is split among all of them.
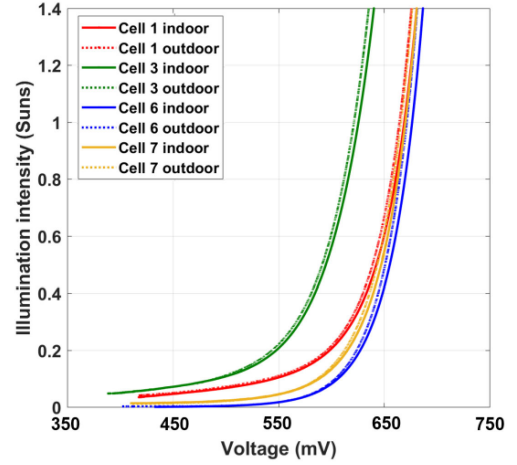
The results obtained using the extended shading method are shown in Fig. 10. The obtained outdoor *I–V* measurements now closely match those obtained indoors. The slight deviations (in the range of 4–5 mV at one Sun) are assumed to be because of temperature differences, as indoor measurements were performed at 25 °C, whereas the outdoor measurements were taken at around 50 °C. This difference can be corrected with the temperature coefficient for Suns-PL measurements, as will be discussed in the next section.

E. Impact of Temperature

Outdoor measurements are naturally taken at a large range of module temperatures. It is thus essential that the analysis is only minimally affected by the different outdoor conditions. In this section, we investigate the effect of temperature on Suns-PL measurements.

Fig. 11(a) presents indoor Suns-V_{oc} and Suns-PL measurements of Cell 6 over the temperature range from 25 to 85 °C. At each temperature, the two measurements are performed simultaneously using uniform heating from a large area halogen lamp. The temperature was measured using an LM35 sensor [61] attached firmly to the back of the tested solar cell.

Over the entire temperature range, the spread of V_{oc} is 128 mV, consistent with a temperature coefficient of ~ -2.13 mV/K. In contrast, the equivalent voltage spread from Suns-PL measurements (iV_{oc}) is only 14 mV, almost one order of magnitude smaller. The evolution of V_{oc} and iV_{oc} as a function of temperature is shown in Fig. 11(b). The difference between V_{oc} and iV_{oc} at 25 °C is observed to be 5 mV, similar to the value reported in [59]. We find a V_{oc} temperature coefficient of -2.1 mV/°C, similar to the values reported in [62]–[65]. The iV_{oc} temperature coefficient (-0.23 mV/°C) is much smaller than the temperature coefficient of V_{oc}, which indicates that Suns-PL measurements are resistant to changes in temperature that are expected during solar power plant operation. The lower iV_{oc} temperature coefficient derives from the luminescence intensity having only a weak temperature dependency for all operating points in the range around room temperature. As $iV_{oc} \propto \ln(\Phi_{PL})$, this dependency
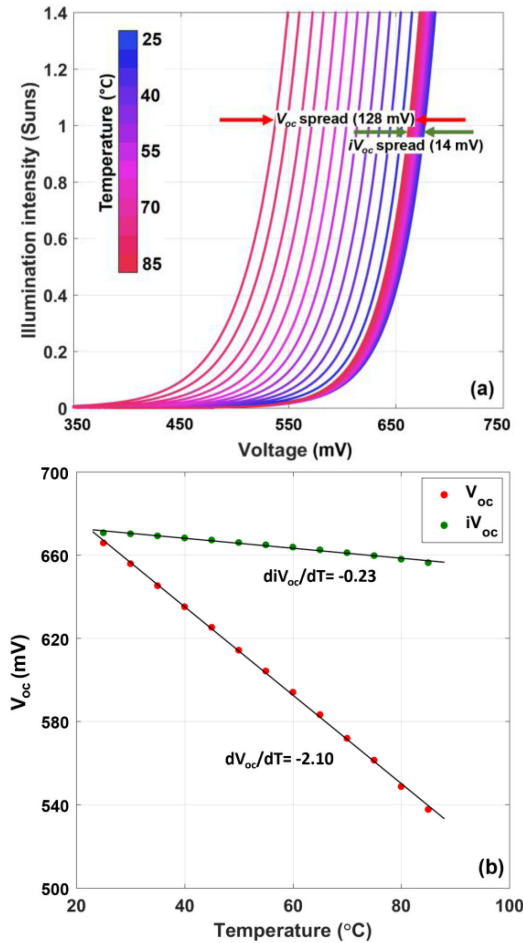
Fig. 11. (a) Measured implied I–V curves obtained by Suns-V_{oc} and Suns-PL at varying module temperatures. (b) V_{oc} and iV_{oc} at one Sun measured as a function of temperature (Cell 6).

is even weaker for iV_{oc}, as discussed by Zafirovska *et al.* [36]. Implied I–V data from Suns-PL are thus found to be extremely robust to temperature variations, which means that only an approximate cell temperature is required to effectively correct for the temperature differences. Such a temperature estimate can, for instance, be conveniently obtained by using a remote infrared thermometer.

IV. CONCLUSION

The Suns-PL measurement technique was successfully applied to investigate solar cells embedded in fully assembled modules operating in outdoor conditions. The method allows contactless extraction of implied I–V curves of individual cells in full daylight. It is sensitive, simple, cost effective, and fast. Information regarding fundamental loss mechanisms, such as recombination current or shunt resistance can, therefore, be easily obtained. Furthermore, the quality of the measurement is sufficient to extract the local ideality factor, a sensitive tool to investigate recombination mechanisms present in solar cells. An easy way to calibrate implied I–V curves was discussed. The effect of measurement artifacts from insufficient shading was investigated and quantified. Measurements confirmed that the

technique is almost unaffected by temperature variations as is expected during outdoor field measurements.

The proposed method can be a very useful and versatile tool for research, as well as, for routine testing during operation and maintenance of solar modules in the field.

REFERENCES

[1] N. M. Haegel *et al.*, "Terawatt-scale photovoltaics: Transform global energy," *Science*, vol. 364, no. 6443, pp. 836–838, 2019.
[2] M. A. Green, "How did solar cells get so cheap?," *Joule*, vol. 3, no. 3, pp. 631–633, 2019.
[3] M. A. Green, "Photovoltaic technology and visions for the future," *Prog. Energy*, vol. 1, no. 1, 2019, Art. no. 013001.
[4] F. Creutzig *et al.*, "The underestimated potential of solar energy to mitigate climate change," *Nature Energy*, vol. 2, no. 9, 2017, Art. no. 17140.
[5] M. A. Munoz, M. C. Alonso-García, N. Vela, and F. Chenlo, "Early degradation of silicon PV modules and guaranty conditions," *Sol. Energy*, vol. 85, no. 9, pp. 2264–2274, 2011.
[6] L. Tinker, R. Jones-albertus, and I. Ave, "Emerging PV technologies : The path to market competitiveness," in *Proc. 43rd IEEE Photovolt. Spec. Conf.*, 2016, pp. 3471–3474.
[7] F. Kersten *et al.*, "Degradation of multicrystalline silicon solar cells and modules after illumination at elevated temperature," *Sol. Energy Mater. Sol. Cells*, vol. 142, pp. 83–86, 2015.
[8] D. N. R. Payne *et al.*, "Acceleration and mitigation of carrier-induced degradation in p-type multi-crystalline silicon," *Phys. Status Solidi - Rapid Res. Lett.*, vol. 10, no. 3, pp. 237–241, 2016.
[9] T. Ishii and A. Masuda, "Annual degradation rates of recent crystalline silicon photovoltaic modules," *Prog. Photovolt. Res. Appl.*, vol. 25, pp. 953–967, 2017.
[10] C. Vargas *et al.*, "Recombination parameters of lifetime-limiting carrier-induced defects in multicrystalline silicon for solar cells," *Appl. Phys. Lett.*, vol. 110, no. 9, Feb. 2017, Art. no. 092106.
[11] S. Pingel *et al.*, "Potential induced degradation of solar cells and panels," in *Proc. 35th IEEE Photovolt. Spec. Conf.*, 2010, pp. 2817–2822.
[12] H. Silva, "PID and LID: Devastating phenomena for PV plants," 2015. Accessed: Feb. 2, 2019. [Online]. Available: https://sinovoltaics.com/quality-control/pid-lid-devastating-phenomena-pv-plants/
[13] J. Lindroos, A. Zuschlag, J. Carstensen, and G. Hahn, "Light-induced degradation variation in industrial multicrystalline PERC silicon solar cells," *AIP Conf. Proc.*, vol. 1999, 2018, Art. no. 130013.
[14] T. Mchedlidze, M. M. Alam, A. Herguth, and J. Weber, "In situ observation of the degradation in multi-crystalline Si solar cells by electroluminescence," *Phys. Status Solidi Appl. Mater. Sci.*, vol. 216, no. 17, pp. 1–9, 2019.
[15] I. Zafirovska, "Line scan photoluminescence and electroluminescence imaging of silicon solar cells and modules," Ph.D. dissertation, Univ. New South Wales, Sydney, NSW, Australia, 2019.
[16] T. J. McMahon, "Accelerated testing and failure of thin-film PV modules," *Prog. Photovolt. Res. Appl.*, vol. 12, no. 2/3, pp. 235–248, 2004.
[17] M. Schütze *et al.*, "Laboratory study of potential induced degradation of silicon photovoltaic modules," in *Proc. 37th IEEE Photovolt. Spec. Conf.*, 2011, pp. 821–826.
[18] J. A. Tsanakas, L. Ha, and C. Buerhop, "Faults and infrared thermographic diagnosis in operating c-Si photovoltaic modules: A review of research and future challenges," *Renewable Sustain. Energy Rev.*, vol. 62, pp. 695–709, 2016.
[19] M. Aghaei, P. Quater, F. Grimaccia, S. Leva, and M. Mussetta, "Unmanned aerial vehicles in photovoltaic systems monitoring applications," in *Proc. 29th Eur. Photovolt. Sol. Energy Conf. Exhib.*, 2014, pp. 2734–2739.

[20] A. Morlier, M. Siebert, I. Kunze, G. Mathiak, and M. Kontges, "Detecting photovoltaic module failures in the field during daytime with ultraviolet fluorescence module inspection," *IEEE J. Photovolt.*, vol. 7, no. 6, pp. 1710–1716, Nov. 2017.

[21] S. Koch *et al.*, "Outdoor electroluminescence imaging of crystalline photovoltaic modules: Comparative study between manual ground-level inspections and drone-based aerial surveys," in *Proc. 32nd Eur. Photovolt. Sol. Energy Conf. Exhib.*, 2016, pp. 1736–1740.

[22] T. Potthoff, K. Bothe, U. Eitner, D. Hinken, and M. Kontges, "Detection of the voltage distribution in photovoltaic modules by electroluminescence imaging," *Prog. Photovolt. Res. Appl.*, vol. 18, pp. 100–106, 2010.

[23] R. Bhoopathy, O. Kunz, M. Juhl, T. Trupke, and Z. Hameiri, "Photoluminescence outdoor measurements of photovoltaic modules under full sunlight illumination," in *Proc. 27th Int. Photovolt. Sci. Eng. Conf.*, 2017, pp. 1–4.

[24] R. Bhoopathy, O. Kunz, M. Juhl, T. Trupke, and Z. Hameiri, "Outdoor photoluminescence imaging of solar panels by contactless switching: Technical considerations and applications," *Prog. Photovolt. Res. Appl.*, vol. 28, no. 3, pp. 217–228, 2020.

[25] P. Sánchez-Friera, M. Piliougine, J. Peláez, J. Carretero, and M. S. de Cardona, "Analysis of degradation mechanisms of crystalline silicon PV modules after 12 years of operation in Southern Europe," *Prog. Photovolt. Res. Appl.*, vol. 19, no. 6, pp. 658–666, Sep. 2011.

[26] J. Schlothauer, S. Jungwirth, M. Kohl, and B. Roder, "Degradation of the encapsulant polymer in outdoor weathered photovoltaic modules: Spatially resolved inspection of EVA ageing by fluorescence and correlation to electroluminescence," *Sol. Energy Mater. Sol. Cells*, vol. 102, pp. 75–85, 2012.

[27] T. Kaden, K. Lammers, and H. J. Möller, "Power loss prognosis from thermographic images of PID affected silicon solar modules," *Sol. Energy Mater. Sol. Cells*, vol. 142, pp. 24–28, 2015.

[28] G. B. Alers, J. Zhou, C. Deline, P. Hacke, and S. R. Kurtz, "Degradation of individual cells in a module measured with differential IV analysis," *Prog. Photovolt. Res. Appl.*, vol. 19, pp. 977–982, 2011.

[29] K. R. McIntosh, "Lumps, humps and bumps: three detrimental effects in the current-voltage curve of silicon solar cells," Ph.D. dissertation, Univ. New South Wales, Sydney, NSW, Australia, 2001.

[30] R. Sinton and A. Cuevas, "A quasi-steady-state open-circuit voltage method for solar cell characterization," in *Proc. 16th Eur. Photovolt. Sol. Energy Conf.*, 2000, pp. 1–4.

[31] A. Killam and S. Bowden, "Characterization of modules and arrays with SunsVoc," in *Proc. 44th IEEE Photovolt. Spec. Conf.*, 2017, pp. 2719–2722.

[32] S. M. F. Zhang *et al.*, "Investigation of HIT module degradation: A postmortem approach," in *Proc. 47th IEEE Photovolt. Spec. Conf.*, 2020.

[33] I. L. Eisgruber and J. R. Sites, "Extraction of individual-cell photocurrents and shunt resistances in encapsulated modules using large-scale laser scanning," *Prog. Photovolt. Res. Appl.*, vol. 4, no. 1, pp. 63–75, 1996.

[34] L. de Bernardez and R. H. Buitrago, "Dark I-V curve measurement of single cells in a photovoltaic module," *Prog. Photovolt. Res. Appl.*, vol. 14, no. 4, pp. 321–327, 2006.

[35] J. Bauer, F. Frühauf, and O. Breitenstein, "Quantitative local current-voltage analysis and calculation of performance parameters of single solar cells in modules," *Sol. Energy Mater. Sol. Cells*, vol. 159, pp. 8–19, 2017.

[36] I. Zafirovska, M. K. Juhl, A. Ciesla, R. Evans, and T. Trupke, "Low temperature sensitivity of implied voltages from luminescence measured on crystalline silicon solar cells," *Sol. Energy Mater. Sol. Cells*, vol. 199, pp. 50–58, 2019.

[37] M. Köntges, M. Siebert, and D. Hinken, "Quantitative analysis of PV-modules by electroluminescence images for quality control," in *Proc. Eur. Photovolt. Sol. Energy Conf.*, 2009, pp. 3226–3231.

[38] R. Bhoopathy, O. Kunz, M. Juhl, T. Trupke, and Z. Hameiri, "Outdoor photoluminescence imaging of photovoltaic modules with sunlight excitation," *Prog. Photovolt. Res. Appl.*, vol. 26, pp. 69–73, 2018.

[39] R. Bhoopathy, O. Kunz, M. Juhl, T. Trupke, and Z. Hameiri, "Inspecting series resistance effects and bypass diode failure using contactless outdoor photoluminescence imaging," in *Proc. 7th World Conf. Photovolt. Energy Convers.*, 2018, pp. 377–380.

[40] R. Bhoopathy, O. Kunz, M. Juhl, T. Trupke, and Z. Hameiri, "A simplified contactless method for outdoor photoluminescence imaging," in *Proc. 46th IEEE Photovolt. Spec. Conf.*, 2019, pp. 2571–2574.

[41] S. Guo, E. Schneller, K. O. Davis, and W. V. Schoenfeld, "Quantitative analysis of crystalline silicon wafer PV modules by electroluminescence imaging," in *Proc. 43rd IEEE Photovolt. Spec. Conf.*, 2016, pp. 3688–3692.

[42] *SCHOTT KG-3 Heat Absorbing Glass*. Accessed: Mar. 5, 2020. [Online]. Available: https://www.edmundoptics.com.au/p/50mm-dia-kg-3-heat-absorbing-glass/9441/

[43] *6675A DC Power Supply*. Accessed: Mar. 5, 2020. [Online]. Available: https://www.keysight.com/en/pd-839263-pn-6575A/2000-watt-power-supply-120v-18a

[44] *SR570 - Low Noise Current Preamplifier*. Accessed: Mar. 5, 2020. [Online]. Available: https://www.thinksrs.com/products/sr570.html

[45] *Measurement Computing USB-1808*. Accessed: Mar. 5, 2020. [Online]. Available: https://www.mccdaq.com/data-acquisition-and-control/simultaneous-daq/USB-1808-Series.aspx

[46] *SPIRE Module Flash Tester*. Accessed: Mar. 5, 2020. [Online]. Available: http://www.eternalsunspire.com

[47] R. A. Sinton, D. de Ceuster, K. Wilson, and L. R. Barbosa, "Flash testing high-efficiency silicon solar cells and modules," in *Proc. 22nd Eur. Photovolt. Sol. Energy Conf.*, Milan, Italy, 2005, pp. 659–662.

[48] M. J. Kerr, A. Cuevas, and R. A. Sinton, "Generalized analysis of quasi-steady-state and transient decay open circuit voltage measurements," *J. Appl. Phys.*, vol. 91, no. 1, pp. 399–404, 2002.

[49] T. Trupke and R. A. Bardos, "Self-consistent determination of the generation rate from photoconductance measurements," *Appl. Phys. Lett.*, vol. 85, no. 16, pp. 3611–3613, 2004.

[50] T. Trupke *et al.*, "Fast photoluminescence imaging of silicon wafers," in *Proc. 4th World Conf. Photovolt. Energy Convers.*, 2006, pp. 928–931.

[51] D. Bredemeier, D. Walter, S. Herlufsen, and J. Schmidt, "Understanding the light-induced lifetime degradation and regeneration in multicrystalline silicon," *Energy Procedia*, vol. 92, pp. 773–778, 2016.

[52] M. Wolf and H. Rauschenbach, "Series resistance effects on solar cell measurements," *Adv. Energy Convers.*, vol. 3, pp. 455–479, 1963.

[53] A. Luque and S. Hegedus, *Handbook of Photovoltaic Science and Engineering*. Hoboken, NJ, USA: Wiley, 2003.

[54] *PV Lighthouse Equivalent-Circuit Calculator*. Accessed: Feb. 20, 2019. [Online]. Available: https://www.pvlighthouse.com.au/equivalent-circuit

[55] O. Kunz, "Evaporated solid-phase crystallised poly-silicon thin-film solar cells on glass," Ph.D. dissertation, Univ. New South Wales, Sydney, NSW, Australia, 2009.

[56] Z. Hameiri, K. McIntosh, and G. Xu, "Evaluation of recombination processes using the local ideality factor of carrier lifetime measurements," *Sol. Energy Mater. Sol. Cells*, vol. 117, pp. 251–258, 2013.

[57] Z. Hameiri and K. R. McIntosh, "On the use of local ideality factor obtained from effective carrier lifetime measurements," in *Proc. 39th IEEE Photovolt. Spec. Conf.*, 2013, pp. 1412–1416.

[58] F. Hernando, R. Gutierrez, G. Bueno, F. Recart, and V. Rodriguez, "Humps, a surface damage explanation," in *Proc. 2nd World Conf. Photovolt. Sol. Energy Convers.*, 1998, pp. 1321–1323.

[59] R. Dumbrell, M. K. Juhl, T. Trupke, and Z. Hameiri, "Comparison of terminal and implied open circuit voltage measurements," *IEEE J. Photovolt.*, vol. 7, no. 5, pp. 1376–1383, Sep. 2017.

[60] T. Trupke, R. A. Bardos, M. D. Abbott, and J. E. Cotter, "Suns-photoluminescence: Contactless determination of current-voltage characteristics of silicon wafers," *Appl. Phys. Lett.*, vol. 87, pp. 2005–2007, 2005.

[61] Texas Instruments LM35. Accessed: Mar. 5, 2020. [Online]. Available: http://www.ti.com/product/LM35

[62] C. Berthod *et al.*, "Temperature sensitivity of multicrystalline silicon solar cells," *IEEE J. Photovolt.*, vol. 9, no. 4, pp. 927–964, Jul. 2019.

[63] C. Berthod, R. Strandberg, G. H. Yordanov, H. G. Beyer, and J. O. Odden, "On the variability of the temperature coefficients of mc-Si solar cells with irradiance," *Energy Procedia*, vol. 92, pp. 2–9, 2016.

[64] D. T. Cotfas, P. A. Cotfas, and O. M. Machidon, "Study of temperature coefficients for parameters of photovoltaic cells," *Int. J. Photoenergy*, vol. 2018, 2018, Art. no. 5945602.

[65] C. Berthod, R. Strandberg, J. O. Odden, and T. O. Saetre, "Reduced temperature sensitivity of multicrystalline silicon solar cells with low ingot resistivity," in *Proc. 43rd IEEE Photovolt. Spec. Conf.*, 2016, pp. 2398–2402.